JOURNAL OF MATERIALS SCIENCE **38** (2003) 1819–1830

Reactor length-scale modeling of chemical vapor deposition of carbon nanotubes

M. GRUJICIC*, G. CAO
Department of Mechanical Engineering, Program in Materials Science and Engineering, Clemson University, Clemson, SC 29634, USA
E-mail: mica.grujicic@ces.clemson.edu

B. GERSTEN
Army Research Laboratory—WMRD AMSRL-WM-MD, Aberdeen, Proving Ground, MD 21005-5069, USA

Chemical Vapor Deposition (CVD) of carbon nanotubes from a gas mixture consisting of methane (carbon precursor) and hydrogen (a carrier gas) in the presence of cobalt, nickel or iron catalytic particles in a cylindrical reactor is modeled at the reactor length-scale by solving a continuum-based coupled boundary-layer laminar-flow hydrodynamics, heat-transfer, gas-phase chemistry and surface chemistry problem. The model allows determination of the gas-phase fields for temperature, velocity, and various species as well as the surface-species coverages and the carbon deposition rate. Various available experimental and theoretical assessments are used to construct the necessary database for gas-phase and surface chemistry and gas-phase transport parameters. A reasonably good agreement is found between the model predicted and the experimentally measured carbon nanotubes deposition rates over a relatively large range of processing conditions.

1. Introduction

Since their discovery in 1991 [1], carbon nanotubes have been the subject of intense research. Single walled carbon nanotubes (SWCNTs) have attracted particular attention because of a wide range of their potential applications. Among these applications are their use: (a) as structural materials with extraordinary mechanical properties [2]; (b) in nano-electronic components [3] in which the limitations imposed by Moore's law may be circumvented [4]; (c) as probes in scanning probe microscopy [5] with the added advantage of a chemically-fuctionalized tip; (d) as high-sensitivity microbalances [6]; (e) as gas detectors [7, 8]; (f) in hydrogen storage devices [9]; (g) as field-emission type displays [10, 11]; (h) as electrodes in organic light-emitting diodes [12] and (i) as tiny tweezers for nanoscale manipulation [13].

Carbon nanotubes are generally processed by laser ablation of carbon rods [e.g., 14], a direct current arc-discharge between carbon electrodes in an inert-gas environment [15] or by chemical vapor deposition (CVD) [16] in combination with nanofabricated catalytic patterning [17] and templating [18]. The aim of these carbon nanotube fabrication processes is the production of long, uniform, single-walled (properties of multi-walled carbon nanotubes, MWCNTs, are quite inferior compared to those of SWCNTs), spatially ordered nanotubes of the same chirality. If the processing conditions are not selected properly, fabricated material typically consists of a mat of poorly ordered entangled SWCNTs and MWCNTs with a distribution in tube diameters with their structure varying between zigzag, armchair and different chiral forms.

Carbon-nanotube modeling efforts can be roughly divided in two distinct categories: (a) Molecular dynamics type calculations employing the Tersoff-Brenner reactive interactive potentials [e.g., 19] and (b) Ab-initio analyses based on density functional total energy calculations [e.g., 20] often combined with molecular dynamics simulations [e.g., 21]. These modeling approaches enable elucidation of the basic mechanisms associated with the growth of SWCNTs and MWCNTs in the absence and in the presence of transition-metal catalysts. However, these methods are unable to help establish relationship between the fabrication-process parameters and the nucleation and growth conditions at the surface of growing nanotubes, the conditions which control microstructure, length and spatial ordering of nanotubes. In a series of papers Grujicic and Lai [22–24] demonstrated that establishment of the process-parameters/growth-conditions/fabricated-material-microstructure relationships entails a multi length-scale approach. That is, the same problem, fabrication of the carbon nanotubes, must be considered at the length scale of a chemical reactor, at the characteristic length-scale of a growing nanotube and at the

*Author to whom all correspondence should be addressed.

atomic length scale. The objective of the present paper is to carry out a reactor length-scale analysis of catalytically-assisted chemical vapor deposition based fabrication of the carbon nanotubes. The results obtained in the present paper are used in a companion paper [25] as input to an atomic-scale analysis of the same fabrication process.

The organization of the paper is as follows. The procedure used to assess and compile various gas-phase and surface chemistry and gas-phase transport properties is described in Section II. A brief overview of the continuum-based coupled boundary-layer laminar-flow hydrodynamics, heat-transfer, gas-phase chemistry and surface chemistry model used to analyze carbon nanotubes fabrication by catalytic thermal decomposition of methane is presented in Appendix. The results obtained in the present work are presented and discussed in Section III. The main conclusion resulted from the present work are summarized in Section IV.

2. Computational procedure

Reactor-scale modeling of the fabrication of carbon nanotubes is carried out for a standard horizontal cylindrical (channel-type) CVD reactor. A model originally developed by Coltrin *et al.* [26] for a laminar boundary-layer two-dimensional (planar or cylindrical) boundary-layer flow based on the known gas-phase and surface kinetic mechanisms for chemically-reacting gas mixtures is used. A brief overview of the model is given in Appendix. The model assumes that diffusive transport is negligible in the principal-flow (x) direction (the direction along the reactor axis) and requires that boundary conditions gas-phase temperature, pressure, velocity in the principal flow direction and the species concentrations be specified at the reactor inlet and at the substrate (reactor walls). For the given geometry of the reactor, the model predicts two-dimensional gas-phase, temperature, velocity and species concentration fields, surface species coverages and the deposition rates.

In the present work, the experimental studies of Buckenstein and Hu [27] and Flahaut *et al.* [28] are closely followed to model fabrication of the carbon nanotubes by catalytic thermal decomposition of methane. Buckenstein and Hu [27] and Flahaut *et al.* [28] used several single transition-metal oxide substrates and binary transition-metal oxide spinel substrates which undergo a hydrogen reduction reaction yielding fine-scale Co, Fe, and Ni based particles. These particles are believed to play a crucial role in promoting the growth of SWCNTs and MWCNTs while preventing their closure by hampering formation of a (fullerene-type) end-cap. Since the objective of the present work is to model the steady-state growth regime of carbon-nanotube deposition and not the initial stage of formation of transition-metal particles, hydrogen reduction of the oxide/spinal substrates and the resulting formation of transition-metal particles are not considered. Instead, such particles are assumed to be present from the onset of carbon-nanotubes deposition. In addition, since the transition metal particles are believed to be attached to the tip of the growing nanotubes (the tip-growth mechanism), they are considered not only to hamper nanotubes closure but also to act as the substrate for carbon absorption/deposition from the gas phase. As a result of an interaction between the gas phase and the substrate, various hydrocarbon species (the products of thermal decomposition of methane) are absorbed on the surface of transition-metal particles. Due to a relatively large size of their molecules, absorbed species are not very mobile on the substrate surface. However, they can readily interact with atomic (gas-phase) hydrogen which gives rise to hydrogen-abstraction. Once hydrogen is completely abstracted from the absorbed hydrocarbons, the resulting surface-absorbed carbon promptly diffuses over the particles surface until it reaches the tip of the growing nanotube to which it readily attaches.

TABLE I A comparison between predicted and experimentally determined [28] carbon-nanotubes growth rates for the case of thermal decomposition of methane at the reactor-wall temperature of 1343 K

	Carbon nanotubes growth rate, μm/min	
Substrate	Model prediction	Experimentally measured [28]
Cobalt	0.11–0.57	0.4–2.4
Nickel	0.11–0.56	0.3–1.6
Iron	0.11–0.55	0.2–0.9

Thirty-four gas-phase reactions in the CH_4-H_2 mixture are considered as summarized in Table I of our recent paper, [29]. The gas-phase reactions involve the following species: CH_4, CH_3, CH_2, CH, C, C_2H, C_2H_2, C_2H_3, C_2H_4, C_2H_5, C_2H_6, H and H_2. Arrhenius kinetic parameters A_i, β_i and E_i which define the temperature dependence of the reaction rate constants, Equation A.11 for all gas-phase reactions are taken from Chemkin II database [29] and could be found also in Table I of [29].

The temperature-dependent transport properties (viscosity, thermal conductivity and the diffusion coefficients) of gas-phase species are also obtained from the Chemkin II database [30]. These quantities were originally obtained from Lennard-Jones parameters for each of the chemical species using standard techniques [37]. Temperature-dependent thermodynamic properties (heat capacities, entropies and enthalpies) for each of the chemical species are also obtained from the Chemkin II database [30]. These data were originally obtained using existing published experimental data and various statistical mechanics estimates based on electronic-structure calculations.

Complex phenomena occurring at the deposition surface involving gas-phase, surface and bulk species are described using surface chemical reactions. Nineteen such reactions are considered in the present work as summarized in Table II in our recent paper, [29]. Symbols G, S and B in the parenthesis following a species name used in [29] to denote respectively whether the species is a gas-phase, a surface or a bulk species are also used in the present paper. Likewise, symbols R, R2 and R3 are used to denote single, double and triple radicals. Twelve surface species: T(S), TH(S), TCH_3(S), TCH_2(S,R), TCH(S,R2), TC(S,R3), TC_2H_2(S), TC_2H(S,R), TC_2(S,R2), TCH_2 CH_3(S), TCHCH_3(S,R), and TCCH_3(S,R2) and one bulk species, C(B), are considered, where symbol T is used to denote the transition-metal (alloy) particle (substrate).

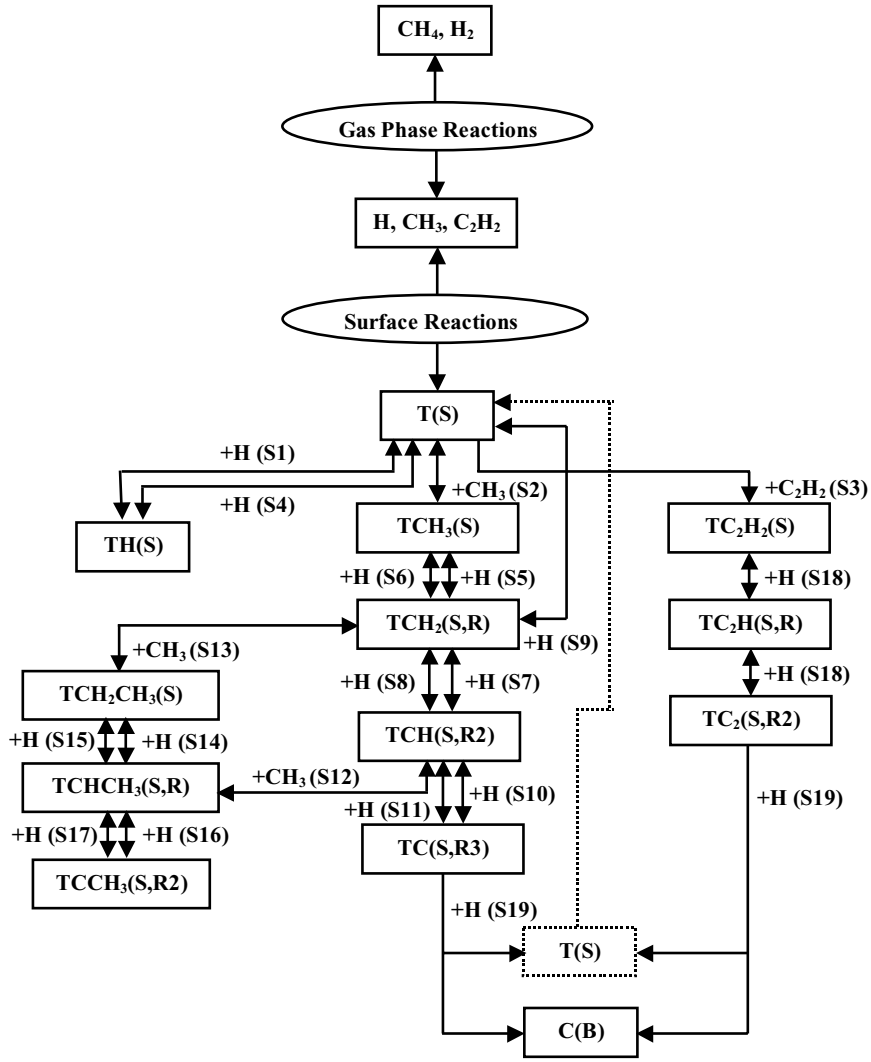

Figure 1 A flowchart of the surface reaction mechanisms involved in CVD of carbon nanotubes form a $CH_4 + H_2$ mixture in the presence of transition-metal catalysts.

A flow chart showing various reaction paths associated with CVD of carbon nanotubes from a $CH_4 + H_2$ mixture in the presence of transition metal particles is shown in Fig. 1. The substrate surface T(S) reacts with gas-phase species H, CH_3 and C_2H_2. Reactions with H lead to passivization of the substrate surface. Reactions with the other two species, on the other hand, give rise to chemisorption of hydrocarbon molecules on to the substrate surface. Through subsequent hydrogen abstraction from the chemisorbed hydrocarbons and from hydrocarbon chemisorbed onto chemisorbed hydrocarbon radicals, TC(S,R3) and TC_2(S,R2) surface species are formed. Since these surface species are, in fact, chemisorbed carbon atoms (and carbon atom pairs), they are quite mobile (in comparison to the chemisorbed large hydrocarbon molecules) and readily diffuse to the growing edges of carbon nanotubes to which they attach. Once a chemisorbed carbon atom attaches to the nanotube edge, a T(S) species (a non-passivated surface site) is created and made available for a continuing chemisorption of hydrocarbon molecules from the gas phase.

The Arrhenius kinetic parameters for various surface reactions listed in Table II of [29] were determined as part of the present work as follows. Reactions S5 ($TCH_3(S) + H \leftrightarrow TCH_2(S,R) + H_2$), S7 ($TCH_2(S,R) + H \leftrightarrow TCH(S,R2) + H_2$), S10 ($TCH(S,R2) + H \leftrightarrow TC(S,R3) + H_2$), S14 ($TCH_2CH_3(S) + H \leftrightarrow TCHCH_3(S,R) + H_2$), S16 ($TCHCH_3(S,R) + H \leftrightarrow TCCH_3(S,R2) + H_2$), and S18 ($TC_2H_y(S,R(2 - y)) + H \leftrightarrow TC_2H_{y-1}(S,R(3 - y)) + H_2$, $y = 1, 2$) involve hydrogen abstraction from the chemisorbed hydrocarbons. Since transition-metal atoms of the substrate surface do not directly participate in these reactions, it is assumed that the rate constants for these reactions are invariant to the nature of the substrate and, hence, the kinetic parameters for the corresponding reactions accompanying CVD of diamond [22] are used. Likewise, transition-metal atoms do not directly participate either in reactions S6 ($TCH_2(S,R) + H \leftrightarrow TCH_3(S)$), S8 ($TCH(S,R2) + H \leftrightarrow TCH_2(S,R)$), S11 ($TC(S,R3) + H \leftrightarrow TCH(S,R2)$), S15 ($TCHCH_3(S,R) + H \leftrightarrow TCH_2CH_3(S)$), and S17 ($TCCH_3(S,R2) + H \leftrightarrow TCHCH_3(S,R)$) which involve chemical reactions between the chemisorbed hydrocarbon radicals and the atomic hydrogen or in reactions S12 ($TCH(S,R2) + CH_3 \leftrightarrow TCHCH_3(S,R)$) and S13 ($TCH_2(S,R) + CH_3 \leftrightarrow TCH_2\ CH_3(S)$) which involve chemical reactions between the chemisorbed hydrocarbon radicals and CH_3. Consequently, the rate constants for these reactions are also assumed to be independent of the character of the substrate and are assigned the

values commonly used for the corresponding surface reactions attending CVD of diamond {22].

Reaction S1 ($T(S) + H \leftrightarrow TH(S)$) involves chemisorption of atomic hydrogen onto the substrate surface and its desorption from it. In accordance with a general practice [e.g., 22], zero activation energy (kinetic parameter E_i in Equation A.11) is assigned to the chemisorption reaction, while the activation energy for desorption is set equal to the absorption energy. Chemisorption energies of H on cobalt (285 kJ/mol), nickel (280 kJ/mol) and iron (295 kJ/mol) as reported in [40] are used. The remaining kinetic parameters for reaction S1 are set equal to their counterparts generally used in the reactor-scale analysis of CVD of diamond [22].

Reaction S2 ($T(S) + CH_3 \leftrightarrow TCH_3(S)$) involves CH_3 chemisorption onto the substrate surface. Again, zero activation energy is assigned to the chemisorption reaction, while the activation energy for desorption is set equal to the absorption energy. CH_3 chemisorption energies on cobalt (144 kJ/mol), nickel (150 kJ/mol) and iron (171 kJ/mol) as determined by Mahalingam *et al.* [39] are used. The remaining kinetic parameters for reaction S2 are set equal to their counterparts generally used in the reactor-scale analysis of CVD of diamond [22].

Reaction S3 ($T(S) + C_2H_2 \leftrightarrow TC_2H_2(S)$) involves chemisorption of C_2H_2. Mahalingam *et al.* [39] showed that due to similarities in the orbital character of CH_3 and C_2H_2, the substrate/carbon bond energies are essentially identical for these two hydrocarbons. Since during chemisorption of CH_3 one substrate/carbon bond is created while two such bonds are formed during chemisorption of C_2H_2, the chemisorption energies of C_2H_2 on cobalt, nickel and iron are two times larger than their CH_3 counterparts. As before, the remaining kinetic parameters for reaction S3 are set equal to their counterparts generally used in the reactor-scale analysis of CVD of diamond [22].

Reaction S4 ($TH(S) + H \leftrightarrow T(S) + H_2$) involves hydrogen abstraction form the (hydrogen) passivated substrate surface. No published data for the kinetic parameters of this reaction are available in the literature. To overcome this problem, reaction S4 is considered as a sum of reverse reaction S1 and the reaction $H + H$ <-> H_2. Since the heats of reaction are known for latter two reactions, the enthalpy changes accompanying reaction S4 are found to be: -162 kJ/mol, -166 kJ/mol and -152 kJ/mol for a cobalt, nickel and iron substrate, respectively. These values are used in the computation of the reverse reaction rate constants whereas the kinetic parameters for CVD of diamond are used to compute the forward rate reaction constants [22].

Reaction S9 ($TCH_2(S,R) + H \leftrightarrow T(S) + CH_3$) involves CH_3 abstraction from the passivated substrate surface covered by chemisorbed $CH_2(S,R)$ radicals. No published data for the kinetic parameters of this reaction are available in the literature. To overcome this problem, reaction S9 is considered as a sum of reverse reaction S2 and forward reaction S6. Since the heats of reaction are known for the latter two reactions, the enthalpy changes accompanying reaction S9 are found to be -205 kJ/mol, -196 kJ/mol and -176 kJ/mol for a cobalt, nickel and iron substrate, respectively. These values are used in the computation of the reverse reaction rate constants whereas the kinetic parameters for CVD of diamond are used to compute the forward rate reaction constants [22].

Reaction S19 ($TC_y(S,R(3 - y)) \leftrightarrow T(S) + yC(B)$, $y = 1, 2$) represents incorporation of the chemisorbed carbon into the growing edge of a carbon nanotube. This reaction is considered as a sum of reverse carbon chemisorption reaction, TC(S,R3) <-> T(S) + C(G), and a graphite condensation reaction, C(G) <-> C(B). Using known heats of reaction for the latter two reactions, the enthalpy change associated with reaction S19 is found to be in a range between -483 and -502 kJ/mol. Such a large negative value of the enthalpy of reaction suggests that reaction S19 is very fast in the forward direction and essentially irreversible. To reflect this finding, an arbitrarily large value of the kinetic parameter A is chosen, Table II of [29]. The computational results are found not to be very sensitive to a two-order increase or decrease in the selected value of A.

3. Results and discussion

The model for chemically-reacting boundary-layer flow presented in Appendix is employed in this section to analyze carbon nanotubes growth from a H_2 + 18 mol% CH_4 mixture at the reactor-wall temperature in a range between 773 and 1023 K and the atmospheric pressure in the presence of cobalt, nickel and iron transition-metal particles. These processing conditions are identical to the ones used in the experimental work of Buckenstein and Hu [27]. The radius of the cylindrical CVD reactor is set to 20 mm, and in order to match the CH_4 flow rate of 20 sccm (standard cm^3/min) used by Buckenstein and Hu [27], the initial axial flow rate u of the gas mixture is set to 90 cm/min. The temperature of the gas mixture at the reactor inlet is set to 573 K.

Contour plots of the gas temperature, the axial velocity, and the molar concentrations of CH_3 and C_2H_2 (the two hydrocarbons whose chemisorption to the substrate surface and subsequent reactions with atomic hydrogen are responsible for carbon nanotubes growth) for the case of CVD at the reactor-wall temperature of 1023 K and in the presence of cobalt catalytic particles are shown in Fig. 2a–d, respectively. Qualitatively similar fields for these quantities are obtained in the cases of carbon nanotube growth in the presence of nickel and iron catalytic particles and at different reactor-wall temperatures. It should be noted that the in Fig. 2a–d, the zero value of the vertical (y) axis (labeled as "Radius") corresponds to the centerline of the reactor while Radius = 2 cm corresponds to the reactor wall.

The temperature field shown in Fig. 2a is as expected, i.e., the gas-mixture heats up as it passes over the hot reactor wall. The axial velocity field shown in Fig. 2b is also as expected, that is as the gas temperature increases, the gas expands and accelerates along

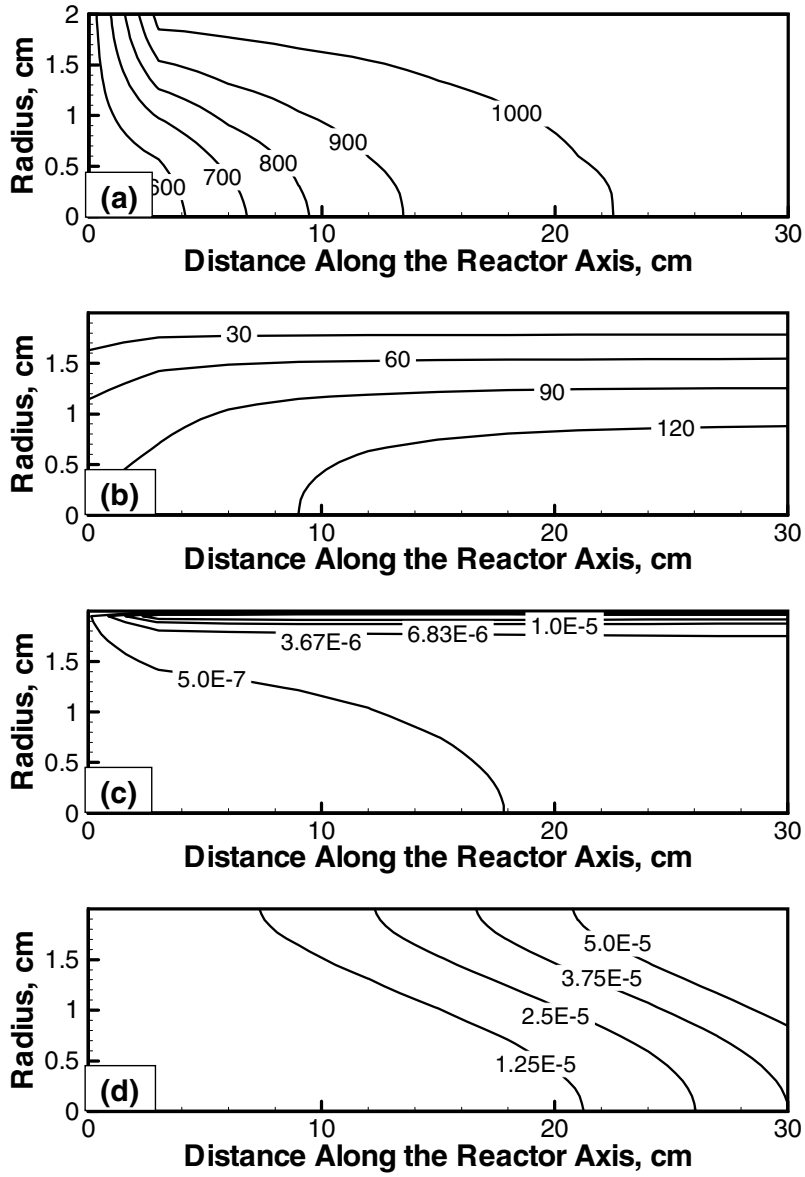

Figure 2 Contour plots of: (a) the gas temperature in K; (b) the axial gas velocity in cm/sec; (c) the CH_3 molar fraction; and (d) the C_2H_2 molar fraction for the case of thermal decomposition of methane at 1023 K (the reactor-wall temperature) in the presence of a cobalt catalyst.

the reactor length. Since CH_3 and C_2H_2 are formed by catalytic thermal decomposition of CH_4, the CH_3 and C_2H_2 concentration fields shown respectively in Fig. 2c and d are controlled by (and are qualitatively similar to) the temperature field. It should be noted that the imposed symmetry (zero-flux) condition across the centerline causes all the contour lines to become vertical at $y = 0$.

Variation of the carbon deposition rate along the length of a 30 cm-long reactor for the case of the reactor-wall temperature of 1023 K and in the presence of cobalt, nickel and iron catalytic particles is shown in Fig. 3. For comparison, the corresponding "steady-state" deposition-rate ranges (denoted as shaded regions) determined experimentally by Buckenstein and Hu [27] are also shown in Fig. 3. For each of the three cases, the computational results show that, as a distance from the reactor inlet increases, the carbon deposition rate first increases (as the gas temperature increases giving rise to catalytic thermal decomposition of CH_4) and later decreases (as the gas mixture becomes depleted on hydrocarbons due to carbon deposition). The computational results are in a good agreement with their experimental counterparts and confirm numerous experimental observations (e.g., 27, 28) that between cobalt, nickel and iron, cobalt is the most effective in promoting formation of carbon nanotubes while iron is the least effective as a catalyst. It should be noted, however, that when Co, Ni and Fe are compared relative to their catalytic effect on promoting the formation of solid carbon, including amorphous carbon, Fe is found to be most effective while Co to be the least effective [42]. These experimental findings have been confirmed computationally in our recent paper [29].

The effect of reactor-wall temperature on the carbon deposition rate in the presence of a nickel catalyst as predicted by the present model is shown as a shaded region in Fig. 4. For comparison, the corresponding experimental results of Buckenstein and Hu [27] are also shown (as solid circles) in the same figure. The agreement between the two sets of results is reasonably good

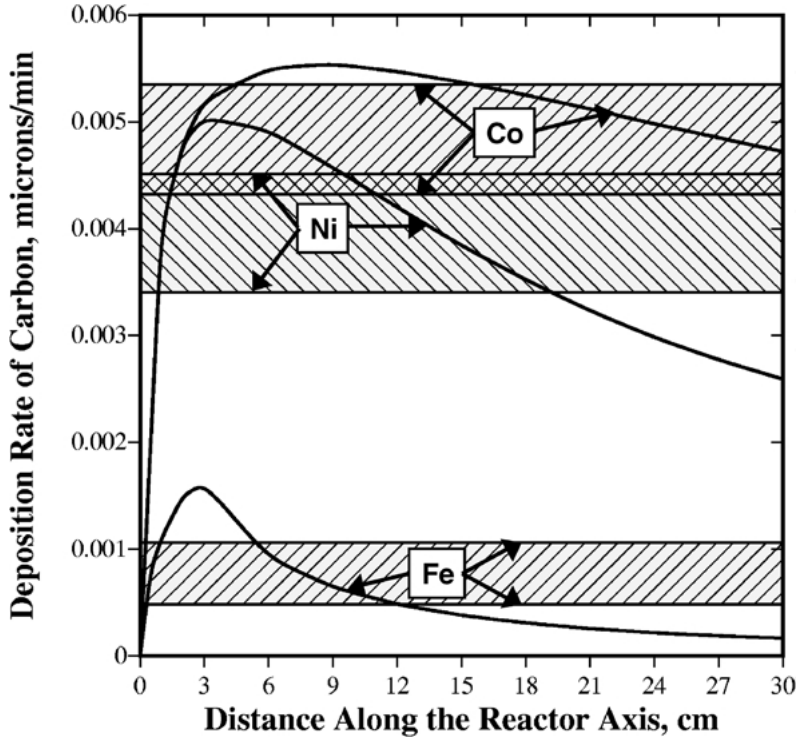

Figure 3 Variation of the carbon deposition rate (solid curves) along the reactor length for the case of thermal decomposition of methane at 1023 K (the reactor-wall temperature) in the presence of a cobalt, nickel or iron catalyst. The shaded regions indicate the experimentally determined ranges of the deposition rates [28].

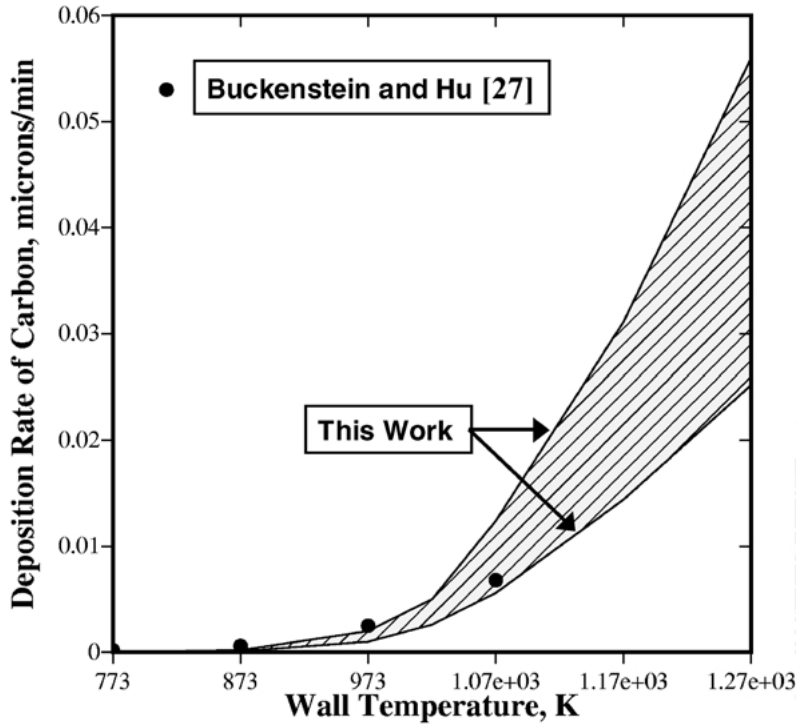

Figure 4 Variation of the T(S) site fraction along the reactor length for the case of thermal decomposition of methane at 1023 K (the reactor-wall temperature) in the presence of a cobalt, nickel or iron catalyst.

in the temperature range in which the carbon nanotubes growth rates are experimentally measured. However, it appears that the experimental growth rates are less temperature sensitive which may give rise to a less satisfactory agreement at higher reactor-wall temperatures. It should be also noted that Buckenstein and Hu [27] measured only the effect of reactor-wall temperature in the transient regime of carbon deposition. Hence, their results had to be rescaled relative to the corresponding steady-state values before they can be compared with the present computational results.

It should be recalled that one of the main assumptions made in the present model is that chemisorbed carbon atoms (formed when the chemisorbed hydrocarbons completely lose their hydrogen through multiple hydrogen abstraction reactions) can readily diffuse

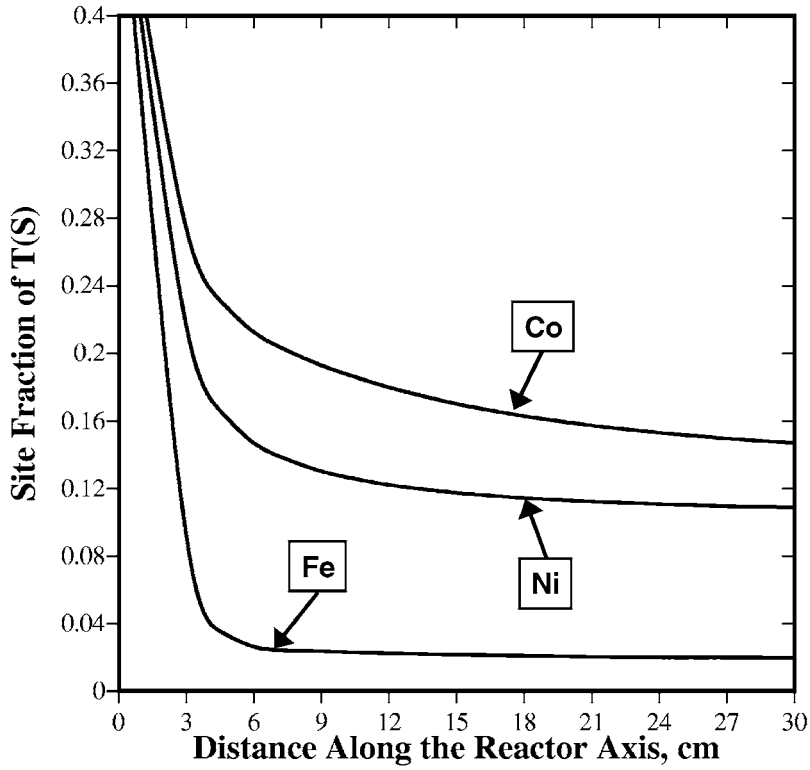

Figure 5 Effect of the reactor-wall temperature on the deposition rate if carbon for the case of thermal decomposition of methane in the presence of a nickel catalyst.

over the substrate surface before reaching the growing edges of carbon nanotubes. For this assumption to be valid, the site fraction of the T(S) surface species has to be significant which then ensures that the probability that chemisorbed carbon atoms ($TC_y(S,R(3-y))$ surface species) have, as their neighbors, a "clean" surface sites is reasonably high. To test validity of the aforementioned assumption, variation of the T(S) site fraction along the length of the reactor for the case of the reactor-wall temperature of 1123 K is shown in Fig. 5. It is seen that for cobalt and nickel catalysts where the T(S) site fractions are in excess of 0.1, it appears justified to assume that surface diffusion of chemisorbed carbon atoms can readily take place. For the case of an iron catalyst, the site fraction of T(S) does not exceed 0.02 and hence the same assumption is less justified. It should also be noted that a comparison of the results shown in Figs 3 and 5 suggests that there is an apparent correlation between the T(S) site fractions and the corresponding carbon deposition rate. That is, the higher is the T(S) fraction (primarily controlled by the magnitude of CH_3 and C_2H_2 chemisorption energies), the higher is the carbon deposition rate. In fact as shown by Mahalingam *et al.* [39], Co, Ni and Fe have among the transition metals the lowest CH_3 and C_2H_2 chemisorption energies which make them the most effective catalysts for carbon nanotubes fabrication by thermal decomposition of methane.

As a final test of the present model, a comparison is made between the computed carbon-nanotubes growth rates and their experimental values at the reactor-wall temperature of 1343 K in the presence of a pure Co, Ni or Fe catalyst as extracted from the work of Flahaut *et al.* [28]. Since the present model allows direct determination of the carbon deposition rate and not the carbon nanotubes growth rate, a relationship between the two rates (both expressed in units of length/time) has to be first established. Such relationship is established in the following way: First it is recognized that the carbon deposition process involves chemisorption of hydrocarbons onto the substrate surface and subsequent hydrogen abstraction while carbon nanotubes growth is controlled by surface diffusion of the chemisorbed carbon and its incorporation in the growing edges of nanotubes. For both processes, however, the rate at which carbon is transferred from the gas phase, expressed as the number of carbon atoms transferred per unit time, is the same. Hence, the product of the carbon deposition rate and the number of carbon-deposition sites on the particle surface must be equal to the product of the carbon nanotube growth rate and the number of nanotube edge sites. From this relationship, one can define a ratio between the nanotube growth rate and the carbon deposition rate for the given particle size (and shape), nanotube radius and the C─C bond length (0.14 nm). Flahaut *et al.* [28] observed SWCNTs with a radius in a 0.4–5 nm range and equiaxed transition metal particles with a radius somewhat larger than that of the associated nanotube. In the present work it is assumed that the particles are spherical and that their size is such that their surface area exposed to be gas mixture (onto which chemisorption of hydrocarbons can take place) is equal to the surface area of a sphere with a radius equal to that for the respective nanotube. Using this procedure, it is found that the nanotube growth rate is between 8 and 40 times larger than the carbon deposition rate depending on the tube (particle) radius. A comparison between the nanotubes growth rates predicted by the

present model and their experimental values extracted from the work of Flahaut *et al.* [28] at the reactor-wall temperature of 1343 K in the presence of a pure Co, Ni or Fe catalyst is given in Table I. The agreement between the two sets of results can be considered as reasonable considering some uncertainty regarding the conversion of predicted carbon deposition rates into nanotubes growth rates and the fact that experimental growth rates (not explicitly reported by Flahaut *et al.* [28]) had to be assessed using SEM images and data for the surface area change accompanying a post-fabrication oxidation treatment. One noticeable difference between the predicted and experimental results is that at high reactor–wall temperatures, the present model predicts that the nature of the substrate (cobalt, nickel or iron) has very little effect on the magnitude of nanotubes growth rates. However, before these discrepancies between the model and the experiment can be considered as deficiencies of the present model at higher wall-temperatures, more reliable experimental data for carbon nanotubes growth rates are needed.

4. Conclusions

Based on the results obtained in the present work the following main conclusions can be drawn;

1. Carbon nanotubes fabrication by cobalt, nickel or iron catalytically-assisted thermal decomposition of methane in a cylindrical reactor has been successfully modeled at the reactor length-scale by solving the appropriate continuum-based coupled boundary-layer laminar-flow hydrodynamics, heat-transfer, gas-phase chemistry and surface chemistry problem.
2. In excellent agreement with experimental observations, it is found that (due to a low magnitude of their chemisorption energies) Co, Ni and Fe are very effective catalysts in comparison with other transition metals and that the catalytic effect is the highest in cobalt, somewhat lower in nickel and still lower in iron.
3. The model predicts carbon deposition rates and carbon nanotubes deposition rates which are in a reasonably good agreement with their experimental counterparts over a relatively large range of processing conditions.

Acknowledgements

The material presented in this paper is based on work supported by the U.S. Army Grant Number DAAD19-01-1-0661. The authors are indebted to Drs. Walter Roy, Fred Stenton and William DeRosset of the ARL for the support and a continuing interest in the present work. The authors also acknowledge the support of the Office of High Performance Computing Facilities at Clemson University.

Appendix A: Model for laminar chemically reacting boundary layer flow

In this section, a brief overview of the coupled hydrodynamic, gas-phase chemistry and surface chemistry model for chemical vapor deposition (and etching) in a boundary-layer laminar-flow channel-type reactor originally developed by Coltrin *et al.* [26] is presented.

A.1 The governing equations

Due to the use of the boundary-layer approximation, the Navier-Stokes equations are reduced to a system of parabolic partial differential equations describing the conservation of mass, momentum, energy, and species composition. The approximation relies on the existence of a principal-flow direction in which diffusive effects can be neglected. The pressure is imposed on the flow by the boundary conditions and is constrained to being uniform in the cross-stream direction. This pressure constraint replaces the cross-stream momentum equation. The governing equations are further modified through the use of Von Mises transformation [31] which replaces the cross-stream coordinate with a stream function. This transformation eliminates the mass conservation equation replacing it with an integral and, in addition, eliminates any explicit reference to the cross-stream convective terms in the resulting governing equations.

Thus, the present model includes the following system of steady-state governing equations:

(a) One (principal-flow direction) momentum conservation equation;

$$\rho u\frac{\partial u}{\partial x}-\frac{\rho u}{M}\left(\xi\frac{\mathrm{d}M}{\mathrm{d}x}-\frac{\mathrm{d}M_l}{\mathrm{d}x}\right)\frac{\partial u}{\partial \xi}+\frac{\mathrm{d}p}{\mathrm{d}x} = \frac{\rho u}{M^2}\frac{\partial}{\partial \xi}\left(\rho u\mu y^{2\alpha}\frac{\partial u}{\partial \xi}\right)+g(\rho_i-\rho) \quad \text{(A.1)}$$

(b) K_g gas-phase species conservation equations;

$$\rho u\frac{\partial Y_k}{\partial x}-\frac{\rho u}{M}\left(\xi\frac{\mathrm{d}M}{\mathrm{d}x}-\frac{\mathrm{d}M_l}{\mathrm{d}x}\right)\frac{\partial Y_k}{\partial \xi} = \dot{\omega}_k W_k-\frac{\rho u}{M}\frac{\partial}{\partial \xi}\left(y^{\alpha}\rho Y_k V_{k_y}\right) \quad (k=1,\ldots,K_g-1) \quad \text{(A.2)}$$

(c) One energy conservation equation;

$$\rho u c_p\frac{\partial T}{\partial x}-\frac{\rho u c_p}{M}\left(\xi\frac{\mathrm{d}M}{\mathrm{d}x}-\frac{\mathrm{d}M_l}{\mathrm{d}x}\right)\frac{\partial T}{\partial \xi} = \frac{\rho u}{M^2}\frac{\partial}{\partial \xi}\left(\rho u\lambda y^{2\alpha}\frac{\partial T}{\partial \xi}\right)-\sum_{k=1}^{K_g}\dot{\omega}_k W_k h_k - \frac{\rho^2 u y^{\alpha}}{M}\sum_{k=1}^{K_g}Y_k V_{k_y} c_{p_k}\frac{\partial T}{\partial \xi} \quad \text{(A.3)}$$

and

(d) One equation of state for the gas phase:

$$p=\frac{\rho RT}{\bar{W}}=\rho RT\sum_{k=1}^{K_g}\frac{Y_k}{W_k} \quad \text{(A.4)}$$

where ρ is the density, u the fluid velocity in the principal-flow (x) direction, M the mass flux, M_l the mass loss (gain) rate at the lower boundary, ξ, the normalized stream function, μ the mixture viscosity, x is

the distance in the principal-flow direction from the reactor inlet, y the cross-stream coordinate, g the gravitational acceleration, ρ_i the density at the reactor inlet, Y_k the mass fraction of kth species, $\sum_{k=1}^{K_g} Y_k = 1$, K_g the total number of gas-phase species, $\dot{\omega}_k$ the rate of production of kth species by gas-phase reactions, W_k is the molecular weight of kth species, c_p the mixture heat capacity, c_{pk} the specific heat capacity of kth species, V_{ky} the diffusion velocity of kth species in the cross-stream (y) direction, λ the mixture thermal conductivity, h_k the specific enthalpy of kth species, p the thermodynamic pressure, R the universal gas constant, T the absolute temperature and $\bar{W}$ the mixture mean molecular weight. The axial coordinate x and the normalized stream function ξ are independent variables while u, T, Y_k, $y^{\alpha+1}$ and p are dependent variables. It should be noted that the last term in Equation A.1 is present only when the gravity vector has a non-zero component along the principal-flow direction.

The diffusion velocity is defined using either a multicomponent transport approach [32]:

$$V_{k_y} = \frac{\rho u y^{\alpha}}{X_k \bar{W} M} \sum_{j \neq k}^{K_g} W_j D_{kj} \frac{\partial X_j}{\partial \xi} - \frac{D_k^T}{\rho Y_k} \frac{\rho u y^{\alpha}}{T M} \frac{\partial T}{\partial \xi} \tag{A.5}$$

or a mixture-average transport method [33]:

$$V_{k_y} = \frac{D_{k,m} \rho u y^{\alpha}}{X_k M} \frac{\partial X_k}{\partial \xi} - \frac{D_k^T}{\rho Y_k} \frac{\rho u y^{\alpha}}{T M} \frac{\partial T}{\partial \xi} \tag{A.6}$$

where $X_k = Y_k \rho / W_k$ is the mole fraction of kth species, D_{kj} the kth/jth species binary diffusion coefficient, D_k^T the thermal diffusion coefficient of kth species, and $D_{k,m}$ the mixture-based diffusion coefficient of kth species.

Following Coltrin *et al.* [26], the mixture-based diffusion coefficient is defined by equating Equations A.5 and A.6 as:

$$D_{k,m} = \frac{\sum_{j \neq k}^{K_g} W_j D_{kj} \left(\partial X_j / \partial \xi \right)}{\bar{W} \sum_{j \neq k}^{K_g} \left(\partial X_j / \partial \xi \right)} \tag{A.7}$$

where the denominator in the last equation is defined by differentiating $\sum_{k=1}^{K_g} X_k = 1$ as:

$$\frac{\partial X_k}{\partial \xi} = - \sum_{j \neq k}^{K_g} \frac{\partial X_j}{\partial \xi} \tag{A.8}$$

It should be noted that while the mixture-averaged transport approximation is computationally less demanding than the full multi-component transport formulation, it may be inadequate for a CVD analysis at very low pressure and in the absence of a carrier gas. It should be also noted that the second term on the right-hand of Equations A.5 and A.6 accounts for the contribution of thermal diffusion to species transport.

The parameter α in Equations A.1–A.3 is equal to 1 for an axisymmetric cylindrical reactor and in this case y represents a radius measured from the reactor axis (flow centerline). The $\alpha = 0$ case corresponds to a reactor consisting of two parallel infinitely-wide plates and y, in this case, represents the distance from the midplane. The rate of production (destruction) of kth species by gas-phase reactions is defined as:

$$\dot{\omega}_k = \sum_{i=1}^{I_g} \nu_{ki} q_i \tag{A.9}$$

where I_g is the total number of gas-phase reactions and ν_{ki} is the net stoichiometric coefficient for kth species in ith reaction. The rate of progress for ith gas-phase reaction is defined as:

$$q_i = k_{fi} \prod_{k=1}^{K_g} X_k^{\nu_{ki}^f} - k_{ri} \prod_{k=1}^{K_g} X_k^{\nu_{ki}^r} \tag{A.10}$$

where ν_{ki}^f and ν_{ki}^r are the forward and the reverse stoichiometric reaction coefficients, respectively. The forward and the reverse rate constants for ith reaction, k_{fi} and k_{ri}, are defined as:

$$k_{fi} = A_i T^{\beta_i} \exp\left(-\frac{E_i}{RT} \right) \tag{A.11}$$

and

$$k_{ri} = \frac{k_{fi}}{K_{Ci}^c} \tag{A.12}$$

where A_i, β_i and E_i are Arrhenius kinetic parameters and K_{Ci}^c is the corresponding concentration-based reaction equilibrium constant. The latter is related to the pressure-based equilibrium constant as:

$$K_{Pi} = K_{ci} \left(\frac{P_{\text{atm}}}{RT} \right)^{\sum_{k=1}^{K_g} \nu_{ki}} \tag{A.13}$$

where P_{atm} denotes the pressure of one standard atmosphere. K_{Pi} can be computed from the appropriate standard-state enthalpy, ΔH_i^o, and entropy, ΔS_i^o, changes accompanying Ith reaction as:

$$K_{Pi} = \exp\left(\frac{\Delta S_i^{\circ}}{R} - \frac{\Delta H_i^{\circ}}{RT} \right) \tag{A.14}$$

Equations A.9–A.14 show that once the gas-phase reactions and their thermodynamic (ΔH_i^o, ΔS_i^o) and kinetic (A_i, β_i and E_i) parameters are defined, the rate of production of kth species $\dot{\omega}_k$ becomes a function of temperature and mass fractions of the gas-phase species.

The stream function is generally defined as:

$$\psi = \frac{1}{\alpha + 1} \int_0^y \rho u \mathrm{d} y^{\alpha+1} \quad \text{or} \quad \frac{\partial y^{\alpha+1}}{\partial \psi} = \frac{\alpha + 1}{\rho u} \tag{A.15}$$

and has the physical meaning that (in the absence of a mass loss/gain) there is an equal mass flow rate between two lines of constant stream function (streamlines). Under such conditions, the reactor walls themselves are streamlines and ψ ranges from zero at lower boundary

(midplane/centerline) to the total mass flux M at the upper one (reactor wall). Also, the total mass (evaluated at the initial conditions) does not change throughout the computation while ψ becomes x-invariant. However, if mass is lost or gained from the gas (due to deposition/etching) the total mass flux changes along the flow direction and a new normalized stream function:

$$\xi = \frac{\psi}{M} \tag{A.16}$$

is defined whose total magnitude ranges between 0 and 1 for the entire problem and is independent of the total mass lost (gained) at the reactor walls. M, in this case, represents the local (x-dependent) value of the total mass flux.

The total local mass flux is generally defined as:

$$\frac{\mathrm{d}M}{\mathrm{d}x} = \frac{\mathrm{d}M_l}{\mathrm{d}x} + \frac{\mathrm{d}M_u}{\mathrm{d}x} \tag{A.17}$$

where the subscripts l and u denote the lower and the upper boundary of the reactor, respectively. For a symmetric planar and an axisymmetric cylindrical reactor, the lower boundary ($y = 0$) coincides with the midplane/centerline where no mass change takes place and, hence, $\mathrm{d}M_l/\mathrm{d}x = 0$. At the upper boundary, i.e., at the reactor wall ($y = y_{\max}$), the change in the mass flux is defined as:

$$\frac{\mathrm{d}M_u}{\mathrm{d}x} = -\rho v y^{\alpha}|_{y=y_{\max}} \tag{A.18}$$

where v is the fluid velocity in y direction.

The initial mass flux at the inlet to the reactor which serves as the initial condition for Equation A.18 is defined as:

$$M_0 = \left(\int_0^{y_{\max}} \rho u y^{\alpha} \mathrm{d}y \right)_{x=0} \tag{A.19}$$

To complete the system of governing equations for the gas phase, the relationship between the cross-stream coordinate and the normalized stream function:

$$\frac{1}{M} \frac{\partial y^{\alpha+1}}{\partial \xi} = \frac{\alpha + 1}{\rho u} \tag{A.20}$$

is defined by differentiating Equation A.15.

As will be discussed in next section, boundary conditions at the reactor wall for the gas-phase species participating in surface-reactions can not be explicitly defined since they are controlled by the extent of these reactions. Instead, these boundary conditions are defined implicitly by the balance between the sum of convective and diffusive mass fluxes of gas-phase species and their production (depletion) rates by surface reactions as:

$$\rho Y_k (V_{k_y} + v) = \dot{s}_k W_k, \quad (k = 1, \ldots, K_g) \tag{A.21}$$

and the cross-flow velocity v is defined by the Stefan condition as:

$$v = \frac{1}{\rho} \sum_{k=1}^{K_g} \dot{s}_k W_k \tag{A.22}$$

where $\dot{s}_k$ is the rate of production of kth gas-phase species by surface reactions. As will be shown below, this quantity depends of the concentrations of gas, surface and bulk species and, hence, the use of Equation A.21 introduces new dependent variables, the concentrations of surface and bulk species. The concentration of each of K_s surface species is defined by the requirement that its steady-state production rate vanishes as:

$$\dot{s}_k = 0, \quad k = 1, .., K_s; \quad \sum_{k=1}^{K_s} z_k = 1 \tag{A.23}$$

where $\dot{s}_k$ is the rate of production of kth species by surface reactions and z_k the site fraction of kth surface species.

The rate of production of kth species by surface reactions $\dot{s}_k$ is defined by an equation analogous to Equation (A.9). The rate-of-progress variable q_i and the forward and the reverse reaction constants, k_{fi} and k_{ri}, for surface reactions are still defined by Equations A.10–A.12, respectively. However, the form of concentration variable X_k in Equation A.10 depends on whether kth species is in the gas phase, (X_k is the molar concentration defined as $Y_k\ \rho/W_k$), on the surface (X_k is the surface molar concentration defined as $z_k \Gamma/\sigma_k$ where Γ is surface site density and σ_k the number of surface sites occupied by kth species) or in the bulk (X_k is the activity a_k and set equal to the mole fraction under the assumption of an ideal solid solution). The pressure-based equilibrium reaction constant is still given by Equation A.14. However, the concentration-based equilibrium constants is now expressed as:

$$K_{Ci} = K_{Pi} \left(\frac{P_{\mathrm{atm}}}{RT} \right)^{\sum_{k=1}^{K_g} \nu_{ki}} (\Gamma^o)^{\sum_{k=1}^{K_s} \nu_{ki}} \prod_{k=1}^{K_s} \sigma_k^{-\nu_{ki}} \tag{A.24}$$

where Γ^o is the standard-state surface site density. Equations A.21–A.25 along with Equations A.9–A.14 show that when surface reactions and their thermodynamic and kinetic parameters are defined, Equations A.21 and A.23 become a set of algebraic equations relating the concentrations of the corresponding gas, surface and bulk species.

The concentration (activity) of the bulk species at the reactor boundary is defined as:

$$a_k = \frac{\dot{S}_k}{\sum_{j=1}^{K_b} \dot{s}_j} \quad k = 1, \ldots, K_b \quad \sum_{k=1}^{K_b} a_k = 1 \tag{A.25}$$

where K_b is the total number of bulk species and $\dot{s}_k$ is treated in the same way as in the case of surface species.

In summary, Equations A.1–A.4, A.17 and A.20 represent a system of $K_g + 4$ equations with $K_g + 4$ unknowns: u, T, Y_k (k = 1,. . ., $K_g - 1$), p, M and $y^{\alpha+1}$. In addition, Equations A.23 and A.25 represent a set of $K_s - 1$ and $K_b - 1$ algebraic equations with $K_s - 1$ z_k and $K_b - 1 a_k$ unknowns, respectively. Once this system of equations is solved, the growth rate for each bulk species is defined as:

$$G_k = \frac{\dot{s}_k W_k}{\rho_k}, \quad k = 1, \ldots, K_b. \tag{A.26}$$

A.2 Boundary conditions

Since the governing equations are parabolic, the boundary conditions for u, T, Y_k, y and p at the reactor inlet ($x = 0$) are defined. It should be noted that, since the x coordinate is time-like from the standpoint of the numerical solution procedure for the system of governing equations, the boundary conditions specified at $x = 0$ can also be considered as initial conditions. It should be noted that for the present differential/algebraic system of equations all initial conditions are not independent. That is, once u, T, Y_k, and p are specified at $x = 0$, the initial conditions for the physical cross-stream coordinate, y, and for the cross-stream velocity, v, are defined form Equation A.15 and from an integral of the mass conservation equation.

As discussed earlier, the midplane/centerline and the reactor wall correspond to streamlines (lines of constant stream function) and, by definition, flow cannot cross these boundaries. Thus, the following boundary conditions are defined at the midplane/centerline $\xi = 0$: $\frac{\partial u}{\partial \xi} = \frac{\partial T}{\partial \xi} = \frac{\partial Y_k}{\partial \xi} = y = v = 0$. At the reactor wall, $\xi = 1.0$, the following boundary conditions are specified: $u = 0$ (no slip condition); $T = T_{\text{wall}}$ or $\partial T/\partial \xi = T'_{\text{wall}}$; $y = y_{\max}$; $\partial Y_k/\partial \xi = 0$ (zero diffusion flux) for the species which do not participate in surface reactions at the reactor wall. The Y_k-boundary conditions for the other species are dependent on the extent of their participation in various surface reactions and, as discussed earlier, is implicitly defined by Equation A.21. It should be noted that overspecification of the boundary conditions for y (two y values are specified even though the governing equation for y, Equation A.15, is of the first order) enables determination of a unique $p(x)$ function (consistent with the initial condition for p at $x = 0$) which accounts for the pressure drop due to shear forces exerted by the reactor wall on the gas mixture.

A.3 Solution procedure

The system of governing equations is treated as a set of differential/algebraic equations [34, 35] and solved using the method of lines. After discretization of the spatial derivatives, numerical solution is obtained using the computer program DASSL [36, 37]. This program solves the equations in a marching fashion starting with the reactor inlet ($x = 0$) and going toward the reactor exit. The program implements a variable step-size based on the backward difference method which makes it very stable and, hence, particularly suited for solution of stiff chemical-kinetics based equations. The general solution approach implemented in DASSL is based on the use of residual functions (equal to zero when the equations are satisfied) which are iterated until the approximate solution (of pre-specified error tolerance) is obtained.

References

1. S. IIJIMA, *Nature* **354** (1991) 56.
2. M. M. J. TREACY, T. W. EBBESEN and J. M. GIBSON, *ibid.* **381** (1996) 678.
3. S. J. TANS, R. M. VERSCHUEREN and C. DEKKER, *ibid.* **393** (1999) 40.
4. G. MOORE, "Every 19 Months, Processing Power Double While Cost Holds Constants" Intel Corporation, 1965.
5. H. DAI, J. H. HAFNER, A. G. RINZLER, D. T. CCBERT and R. E. SMALLEY, *Nature* **384** (1996) 147.
6. PH PANCHARAL, Z. L. WANG, D. UGARTE and W. DE HEER, *science* **283** (1999) 1513.
7. J. KONG, *ibid.* **287** (2000) 622.
8. P. G. COLLINS, K. BRADLEY, M. ISHIGAMI and A. ZEATL, *ibid.* **287** (2000) 1801.
9. A. C. DILLON, *Nature* **386** (1997) 377.
10. Q. H. WANG, *Appl. Phys. Lett.* **72** (1998) 2912.
11. M. GRUJICIC, G. CAO and B. GERSTEN, *Applied Surface Science*, 2002, in press.
12. C. J. LEE, *Appl. Phys. Lett.* **75** (1999) 1721.
13. P. KIM and C. M. LIEBER, *Science* **285** (1999) 2140.
14. A. THESS, *ibid.* **273** (1996) 483.
15. S. IIJIMA and T. ICHIHASHI, *Nature* **363** (1993) 609.
16. R. ANDREWS, *Chem. Phys. Lett.* **303** (1999) 467.
17. M. TERRONES, *Nature* **388** (1997) 52.
18. J. LI, C. PAPADOPOULOS, J. M. XU and M. MCISKOVITS, *Appl. Phys. Lett.* **75** (1999) 367.
19. A. MAITI, C. J. BRABEC, C. ROLAND and J. BERNHOLC, *Phys. Rev.* **52** (1995) 14850.
20. Y. H. LEE, S. G. KIM and D. TOMANEK, *Phys. Rev. Lett.* **24** (1997) 2393.
21. J.-C. CHARLIER, A. D. VITA, X. BLASÉ and R. CAR, *Science* **275** (1997) 646.
22. M. GRUJICIC and S. G. LAI, *J. Mater. Sci.* **35** (2000) 5359.
23. *Idem.*, *ibid.* **35** (2000) 5371.
24. *Idem.*, *Journal of Materials Synthesis and Processing* **8** (2000) 73.
25. M. GRUJICIC, G. CAO and B. GERSTEN, *Mater. Sci, and Eng.* B **B94** (2002) 247.
26. M. E. COLTRIN, R. J. KEE and J. A. MILLER, *J. Electrochem. Soc.* **131** (1984) 425; *Idem.*, *ibid.* **133** (1986) 1206.
27. E. BUCKENSTEIN and Y. H. HU, *Carbon* **36** (1998) 275.
28. E. FLAHAUT, A. GOVINDARAJ, A. PEIGNEY, CH. LAURENT, A. ROUSSET and C. N. R. RAO, *Chem. Phys. Lett.* **300** (1999) 236.
29. M. GRUJICIC, G. CAO and B. GERSTEN, *Applied Surface Science* **191** (2002) 239.
30. R. J. KEE, F. M. RUPLEY and J. A. MILLER, Sandia National Laboratories Report SAND89-8009 (1989).
31. F. K. MOORE (ed), "Theory of Laminar Flows," Vol. IV, "High Speed Aerodynamics and Jet Propulsion," (Princeton University Press, Princeton, NJ, 1964).
32. G. DIXON-LEWIS, in "Combustion Chemistry," edited by W. C. Gardener (Springer-Verlag, New York, 1984) p. 21.
33. M. E. COLTRIN, R. J. KEE, and J. A. MILLER, Sandia National Laboratories Report, SAND90-8003 (1990).
34. R. J. KEE and L. R. PETZOLD, Sandia National Laboratories Report, SAND86-8893, 1986.
35. R. J. KEE, L. R. PETZOLD, M. D. SMOOKE and J. F. GREAR, in "Multiple Time Scales," edited by J. U. Brackhill and B. I. Cohen (Academic Press, San Diego, 1985) p. 113.
36. L. R. PETZOLD, Sandia National Laboratories Report, SAND82-8637 (1982).

37. K. E. BRENAN, S. L. CAMPBELL and L. R. PETZOLD (eds.), "Numerical Solution of Initial-Value Problems in Differential-Algebraic Equations," (North-Holland, New York, 1989).
38. R. J. KEE and J. A. MILLER, Sandia National Laboratories Report, SAND81-8241 (1981).
39. P. MAHALINGAM, H. LIU and D. S. DANDY, *Chem. Phys. Lett.* **29** (1996) 283.
40. D. O. HAYWARD and B. M. W. TRAPNELL, *"Chemisorption"* (Butterworth, London, 1964).
41. M. E. COLTRIN and D. S. DANDY, *J. Appl. Phys.* **74**(9) (1993) 5803.
42. A. GOVINDARAJ, E. FLAHAUT, CH. LAURENT, A. PEIGNEY, A. ROUSSET and C. N. R. RAO, *J. Mater. Research* **14** (1999) 2567.

Received 19 September 2001
and accepted 13 January 2003